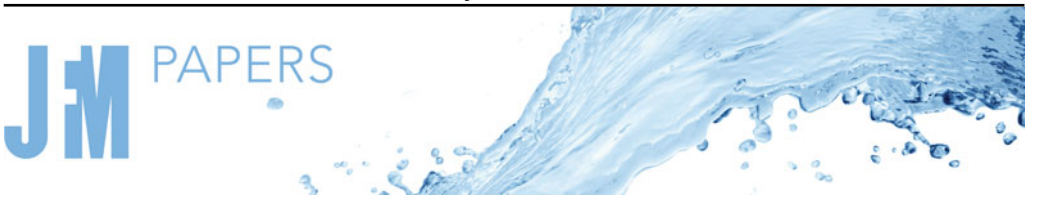
J. Fluid Mech. (2025), *vol.* 1025, A31, doi:10.1017/jfm.2025.10982



Experimental investigation of surfactant effects on gravity–capillary wave dissipation and surface flow

Chang Xu[1] **and Marc Perlin**[1]

[1]Department of Ocean Engineering, Texas A&M University, College Station, TX, USA

Corresponding author: Chang Xu, xuchang@tamu.edu

(Received 23 July 2025; revised 10 November 2025; accepted 21 November 2025)

Sea surface films significantly influence air–sea interaction. While their damping effect on gravity–capillary waves is well recognised, the detailed mechanisms by which surface films alter small-scale wave dynamics – particularly energy dissipation and near-surface flow patterns – remain insufficiently understood. This paper presents experimental observations focusing on small-scale wave profiles and surface-flow dynamics in the presence of surfactants, providing direct experimental evidence of underlying mechanisms such as Marangoni effects. The experiments demonstrate enhanced energy dissipation and significant alterations in near-surface flow caused by surfactants, including the transformation of typical circular motion into elliptical-like trajectories and the emergence of reverse surface drift.

Key words: waves/free-surface flows, capillary waves, thin films

1. Introduction

Sea surface films are thin layers of material that accumulate at the ocean's surface. These films are composed of various substances, including organic matter, microbial aggregates and pollutants such as hydrocarbons. This makes the sea surface microlayer, having a thickness ranging from 1 to 1000 μm, possess physicochemical and biological characteristics that differ from the waters beneath. One significant component of sea surface films is surfactants. Surfactants are molecules that can lower the surface tension of a liquid, in this case, the ocean water. Recent research indicates that, given their extensive distribution across the ocean's surface, the influence of these elements on air–sea interactions may exert a substantial effect on wave dynamics, climatic patterns and additional environmental processes (Martínez-Vicente *et al.* 2019; Ferrero *et al.* 2022).

© The Author(s), 2025. Published by Cambridge University Press. This is an Open Access article, distributed under the terms of the Creative Commons Attribution licence (https://creativecommons.org/licenses/by/4.0/), which permits unrestricted re-use, distribution and reproduction, provided the original article is properly cited.

https://doi.org/10.1017/jfm.2025.10982 Published online by Cambridge University Press

The influence of surfactants is particularly pronounced in capillary and gravity–capillary waves. For example, surfactants are known to suppress capillary waves, creating smoother sea-surface areas that manifest as dark regions in synthetic aperture radar (SAR) imagery. This phenomenon has attracted interest from the remote sensing community (Sobhani, Siadatmousavi & Mehdinia 2024) in tracking pollutants on the sea surface. Also, surfactants on the sea surface can cause significant modifications to the air–sea boundary layer. These modifications can result in changes in drag and enthalpy exchange coefficients, which are crucial for estimating wind-generated waves. Benetazzo *et al.* (2019) demonstrated that surfactant layers significantly dampen short gravity–capillary waves, reducing wave amplitudes and altering wind stress distributions at the ocean surface. Cox, Zhang & Duda (2017) illustrated how polar oil films can suppress large wave breakers by modulating energy flux into ocean waves and altering boundary-layer airflow dynamics. A numerical study by Matsuda *et al.* (2023) found that wind waves grow faster and have greater heights under low surface tension than under higher surface tension. Nevertheless, lab experiments by Sun *et al.* (2023) indicate that surfactants significantly suppress wave generation by reducing the wind stress and by increasing damping. Some of these results are somewhat contradictory, suggesting that research in this area is in its very early stages, and the exact mechanisms through which surface films influence wave generation, dissipation and surface flow patterns at small scales have not been studied extensively.

Due to the minuscule size of the surfactant layer and its elusive nature, achieving a comprehensive understanding of the underlying physics remains challenging. While analytical models, such as the Boussinesq–Scriven model (Shen *et al.* 2018) and numerical models for surface tension and surfactant effects exist across various methods (Popinet 2018) (e.g. volume of fluid (VOF), level set, front tracking, lattice Boltzmann), these models often rely on simplified assumptions, for example, adding a curvature-proportional surface force term to represent surface tension, while neglecting the effect of surface-tension gradients that arise under surface deformation. Large-scale experiments have been reported in the literature. For example, Sergievskaya *et al.* (2019) studied the damping effect of oil films on the sea surface and found that crude oil floating on the water significantly enhances wave damping. Rajan (2020) developed a three-fluid surfactant interface (TFSI) model to analyse damping of internal waves, accounting for the rotational motions in the shear layers, fluid viscosity and interface elasticity. They also measured the damping rates of gravity waves on water beneath a thick oil layer, and found the experimental results fit well with the TFSI model. There is, however, a need for small-scale experiments that can provide evidence of physical explanations of surfactant effects on gravity–capillary waves. Most of the previous experiments only measure the wave profiles. The authors' own work (Xu & Perlin 2023) measured wave generating and damping rates, including quantifying the detailed near-surface flow information.

Measuring the near-surface flow field and related properties has long been a challenge. The complexity arises from the small-scale nature of the experiments, and the close connection between surface viscosity and Marangoni effects, as highlighted in various studies (Levich & Krylov 1969; Langevin 2014). Previous studies have shown that Marangoni stresses significantly influence wave dynamics. Panda *et al.* (2025) reported numerical evidence of altered pattern formation in Faraday waves, while Strickland, Shearer & Daniels (2015) experimentally measured the redistribution of insoluble surfactants on gravity–capillary waves. To the best of the authors' knowledge, however, no prior experiments have directly visualised or quantified the flow patterns induced by surfactants in propagating waves, nor the associated dissipation. Available experimental data typically provide information about the surface and bulk phases simultaneously,

https://doi.org/10.1017/jfm.2025.10982 Published online by Cambridge University Press

making it difficult to extract specific surface-related details before establishing a delicate surface wave model. Accordingly, a high-resolution flow-field measurement is necessary to determine the physics by which changes occur to surfactants on gravity–capillary and capillary waves.

To advance the understanding of these processes, this paper presents experimental observations focusing on small-scale wave profiles and surface-flow dynamics in the presence of surfactants. The study examines enhanced energy dissipation and alterations in near-surface flow caused by surfactants, providing direct experimental evidence of underlying mechanisms such as Marangoni effects. These findings offer new insights into the fundamental physics of wave–surface film interactions and will contribute to improved modelling of air–sea exchanges influenced by surfactants.

2. Methodology

2.1. *Water treatment and surfactants*

The water used in this study is distilled water. The surfactant is Triton X-100, a clear liquid with a viscosity of approximately 270 centipoise at 25 °C, which is soluble in water at room temperature. Two surface conditions are considered: 'clean water' refers to distilled water; 'TX-100' refers to distilled water mixed with Triton X-100. The Triton X-100 is first dissolved in stock water solutions, which are diluted into the bulk water of the tank (350 mm $\times$ 170 mm) to achieve target concentrations. The solutions are gently mixed and allowed to rest for one minute prior to each experiment to promote interfacial adsorption of surfactant molecules. A longer waiting period increases the likelihood that the exposed water surface becomes contaminated by airborne impurities, leading to measurable changes in surface tension (Ponce-Torres, Vega & Montanero 2016). The prepared surfactant solutions had mass concentrations of $0.036\,\mathrm{g\,l^{-1}} \pm 0.005\,\mathrm{g\,l^{-1}} \approx 28.8\,\mu\mathrm{M}$ and $0.018\,\mathrm{g\,l^{-1}} \pm 0.008\,\mathrm{g\,l^{-1}} \approx 59.2\,\mu\mathrm{M}$, based on the precision of the instruments used during preparation. Triton X-100 remains well below its critical micelle concentration (CMC), which is approximately 0.2–0.3 mM according to Sigma-Aldrich (2025), ensuring that the surfactant resides predominantly at the air–water interface rather than forming micelles in the bulk. Although the associated uncertainties are relatively large, these concentrations are sufficient to clearly reveal the influence of surfactants on surface motion and dissipation, which is the primary aim of these experiments.

2.2. *Wave-profile measurement*

Free-surface synthetic Schlieren (FS-SS), initially introduced by Moisy, Rabaud & Salsac (2009), provides non-intrusive measurements of free-surface wave profiles. The experimental set-up of FS-SS is shown in figure 1. In this study, a random dot pattern is placed beneath the transparent tank, that is captured by a high-speed camera positioned above the water surface. To minimise wall friction, the tank sidewalls are covered with nano-silica–coated Polyethylene terephthalate film to increase hydrophilicity. Waves are generated using an electrodynamic shaker (Modal Shop, Model 2110E), allowing precise control over wave frequency and amplitude. A plunger-type wavemaker is installed at one end of the tank and driven by the electrodynamic shaker operating at excitation frequencies of 12 Hz, 24 Hz and 36 Hz. A high-speed camera (Phantom VEO340L) equipped with a 50 mm f/1.8D lens (Nikon AF Nikkor) and operating at 1000 frames per second is positioned above the tank to record distortions of the random dot pattern placed beneath the transparent tank bottom. The camera field of view is 120 mm by 70 mm over the free surface. The procedure for obtaining free-surface measurements using the FS-SS technique is as

https://doi.org/10.1017/jfm.2025.10982 Published online by Cambridge University Press

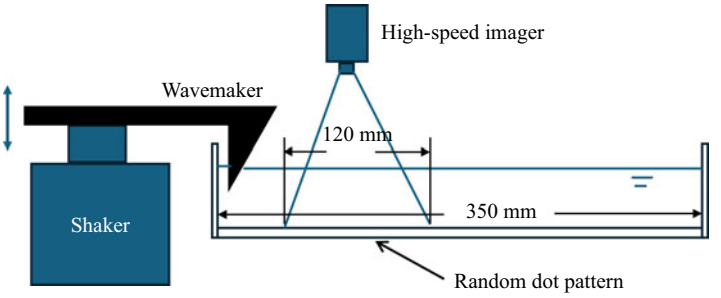


Figure 1. Experimental set-up for the FS-SS method.

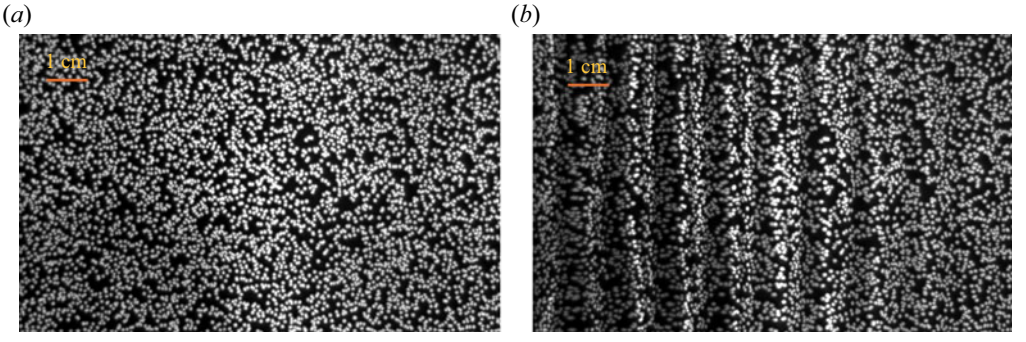


Figure 2. Sample images captured using the FS-SS method: (*a*) still water, (*b*) water with mechanically generated waves at 24 Hz. Surface distortions cause refraction, leading to visible distortion of the dot pattern beneath the transparent tank.

follows. First, a reference image of the random dot pattern is recorded with a quiescent water surface (figure 2*a*. Next, the shaker is set to the desired frequency and peak-to-peak stroke. The distorted random pattern, caused by refraction from surface disturbances, is then captured using a high-speed camera (figure 2*b*). A digital image correlation (DIC) algorithm is applied to compute the displacement field of the dot pattern. Finally, using this displacement field and the calibration reference, FS-SS reconstructs the free-surface elevation, η, for each frame captured by the high-speed camera (see details in Moisy *et al.* 2009). In this way, both temporal and spatial measurements of the water surface are obtained. The FS-SS method has been substantiated as an effective means for reconstructing two-dimensional gravity–capillary wave elevations, as long as the wave steepness is not too large, and the detailed set-up can be seen in the authors' previous work (Xu & Perlin 2021).

2.3. *Surface-flow measurement*

Particle image velocimetry (PIV) provides detailed measurements of the velocity fields beneath wave surfaces. In this study, glass hollow spheres (9–13 μm diameter, density of 1.1 g cm^{-3}) are used as tracer particles. A laser sheet (532 nm wavelength) illuminates these particles, with images captured by the high-speed imager. Velocity fields are determined from sequential images using advanced DIC algorithms implemented through LaVision DaVis software. The experimental set-up for PIV is shown in figure 3. This analysis yields detailed velocity fields beneath the water surface, enabling understanding of the mechanism of wave dissipation. In this study, images recorded using PIV are

https://doi.org/10.1017/jfm.2025.10982 Published online by Cambridge University Press

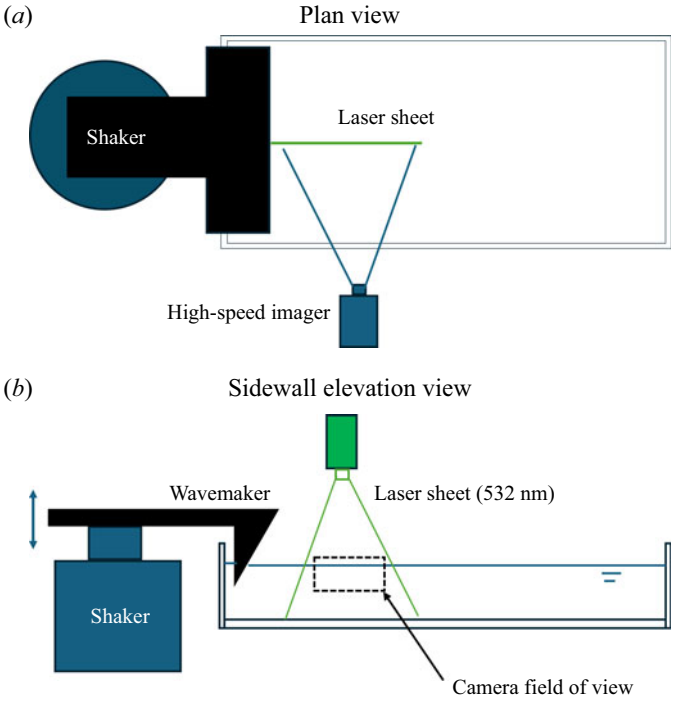


Figure 3. Experimental set-up for PIV: (*a*) plan and (*b*) sidewall elevation views.

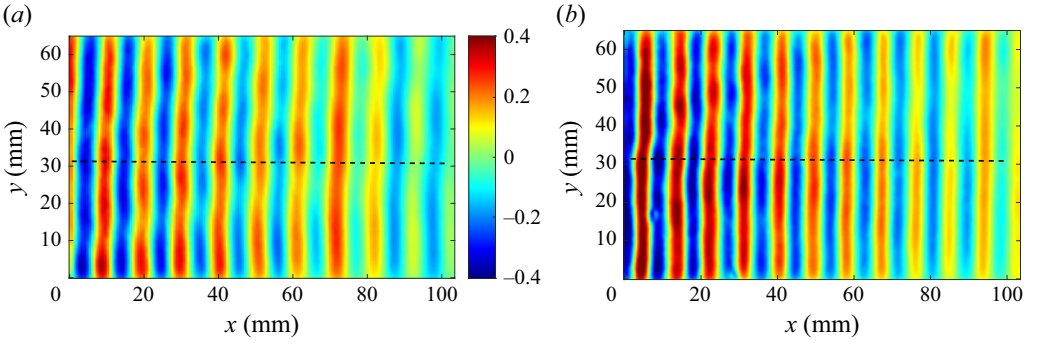


Figure 4. Two-dimensional surface reconstruction for 24 Hz waves using the FS-SS method: (*a*) clean surface, (*b*) with Triton X-100. Dashed lines indicate the locations of the two-dimensional wave-profile extraction.

also used to analyse the free-surface flow patterns by tracking the trajectories of surface particles. The detailed approach is described in § 3.3.

3. Results and discussions

3.1. *Surface wave profiles*

Three wave frequencies are examined in this study: 12 Hz, 24 Hz and 36 Hz, with and without surfactant. The reconstructed free surfaces using FS-SS for 24 Hz waves with and without surfactant are shown in figure 4. As illustrated in the figure, the FS-SS method achieves a two-dimensional free-surface measurement. Two-dimensional spatial

https://doi.org/10.1017/jfm.2025.10982 Published online by Cambridge University Press

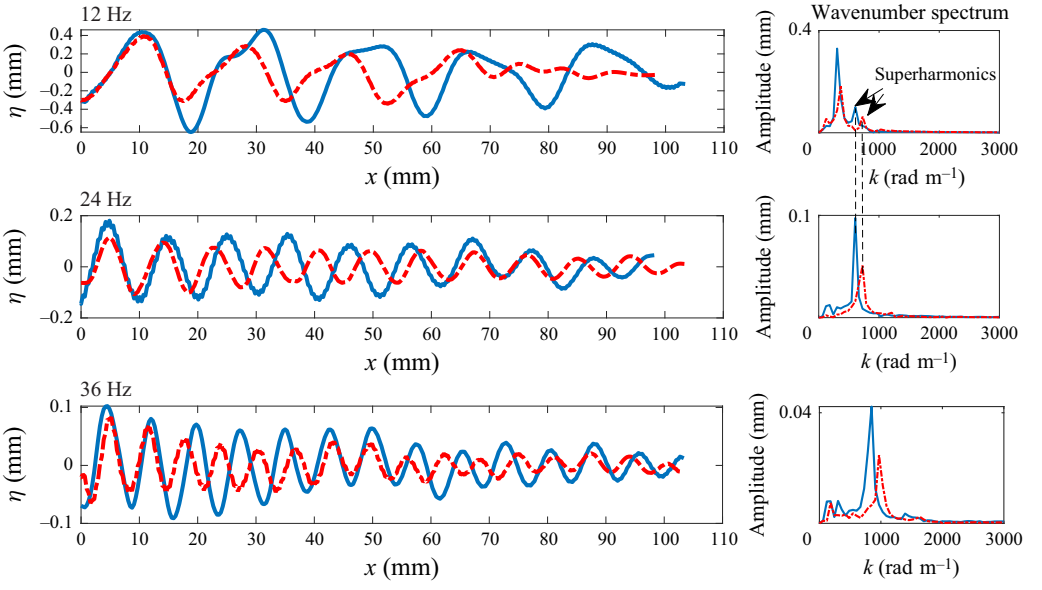


Figure 5. Wave profiles and wavenumber spectra. Blue solid lines, clean water; red dashed lines, water with Triton X-100. (The ordinate scales vary on these figures).

wave profiles are then obtained from the surface reconstruction. The results are obtained by extracting the wave elevations along the central positions (dashed lines in figure 4), which correspond to the locations furthest from the sidewalls and thus minimises sidewall effects. As plane waves are generated in the wave tank, two-dimensional wave profiles provide a suitable basis for evaluating wave dissipation, and the results are shown in figure 5. For accuracy of the method, see Xu & Perlin (2021). It can be seen, in all cases, that the addition of surfactants leads to a reduction in wavelength, consistent with the dispersion relation for gravity–capillary waves: $\omega^2 = gk + (Tk^3/\rho)$, where ω is the angular frequency, g is the gravitational acceleration, k is the wavenumber, T is the surface tension, and ρ is the fluid density. Spatial wave attenuation is evident across all frequencies in figure 5, with the 36 Hz waves exhibiting almost complete dissipation before reaching the end of the tank. As shown in the following section, the 12 Hz waves on clean water decay to approximately 10 % of their initial amplitude when they reach the end of the tank, while cases with surfactants and higher frequencies exhibit even stronger attenuation and barely persist to the tank's end. Moreover, 12 Hz measurements were performed before the waves reached the far end of the tank, thereby eliminating any potential reflection effects. For example, the group velocity of 12 Hz waves in clean water is 21.5 cm s^{-1}, thus it takes approximately 1.6 s for the wave energy to reach the end of the tank. To eliminate the initial transient phase, measurements were performed in the interval $t = 1$ s to $t = 1.5$ s. For higher frequencies and for cases with surfactants, measurements are conducted after the initial transient phase. In these cases, reflections are not a concern, as the wave energy undergoes strong attenuation and decays substantially before reaching the end of the tank. Figure 5 indicates that the presence of surfactants leads to an enhanced spatial dissipation, with the effect becoming more pronounced at higher wave frequencies. This trend is attributed to the increasing influence of surface tension and Marangoni effects as the wavelength decreases. It should be noted that the 12 Hz waves do not exhibit a sinusoidal waveform. This deviation is attributed to the presence of a superharmonic component, resulting from weak nonlinearity in the system. A small dip can be observed

https://doi.org/10.1017/jfm.2025.10982 Published online by Cambridge University Press

in each wave cycle. The superharmonic components are also evident in the wavenumber spectrum and are aligned with the 24 Hz peaks. The wavenumber spectrum is obtained by applying a spatial Fourier transform to the wave profile. In the FS-SS measurements in the present study, the spatial resolution is 0.33 mm, which, according to the Nyquist sampling theorem, limits the maximum resolvable wavenumber to approximately 10 000 rad m^{-1}.

3.2. *Enhanced dissipation by surfactants*

Energy dissipation is typically characterised in the temporal domain, with wave attenuation primarily attributed to the intrinsic viscosity of water. In this study, we establish a connection between temporal dissipation and the spatial attenuation observed in the experiments. Lamb (1924) describes the temporal decay of wave amplitude due to viscosity using the following:

$$\eta(x,t) = \eta_0 \mathrm{e}^{\mathrm{i}(kx-\omega t)-2\nu k^2 t}, \tag{3.1}$$

where η_0 is the initial wave amplitude, and ν is the kinematic viscosity. By relating the spatial coordinate to time through the relation $x = c_g t$, where c_g is the group velocity, and substituting c_g for gravity–capillary waves into (3.1), the expression yields

$$\eta(x,t) = \eta_0 \mathrm{e}^{\mathrm{i}(kx-\omega t)-\xi_t x}, \tag{3.2}$$

with the theoretical exponential decay rate (Crapper 1984)

$$\xi_t = \frac{4\nu k^3}{\omega}\frac{1+\frac{Tk^2}{\rho g}}{1+\frac{3Tk^2}{\rho g}}. \tag{3.3}$$

To compute the theoretical spatial decay rate, the wavenumber k is extracted from the measured wave profiles, and the surface-tension values T are solved from the dispersion relation. For clean water, the surface tension is determined to be 0.074 N m^{-1}, whereas for water with Triton X-100 added, the surface tension decreases to 0.043 N m^{-1}. (Note that the slightly larger than usual value of surface tension for clean water is calculated using the FS-SS measured wavelengths, and it is then averaged over the 12 experiments.) The measured value of 0.043 N m^{-1} is reported here as a reference effective surface tension of the surfactant solution. It should be noted that under wave propagation, the surfactant distribution along the interface becomes variable, leading to local and time-dependent differences in surface tension that drive the Marangoni flow. Direct measurement of the dynamic surface tension field is beyond the scope of the present experimental set-up; nevertheless, the reported value provides a useful reference for characterising the surfactant-laden interface. These values are assumed to remain consistent across all clean-water cases and across all surfactant cases.

Peak values extracted from the wave elevations (see figure 5) are used to estimate the measured spatial decay rate, ξ_m, using the expression $m\lambda\xi_m = \ln(\eta_n/\eta_{n+m})$, where η_n is the peak value of the nth wave crest, η_{n+m} is the peak amplitude of the crest m wavelengths downstream, and λ is the wavelength. The comparison of theoretical and experimental spatial decay rates is shown in table 1. As shown in the table, the measured decay rates are significantly higher than the theoretical ones. This discrepancy may be attributed to sidewall contact line friction and the nonlinear nature of the generated waves. As the theoretical decay rate is derived from linear wave theory, nonlinear effects inherently lead to enhanced dissipation, causing the theoretical prediction to systematically underestimate the actual dissipation rate. Table 1 also shows that the presence of surfactants increases the decay rate. Interestingly, while theoretical values suggest that smaller-scale waves

https://doi.org/10.1017/jfm.2025.10982 Published online by Cambridge University Press

Exciting frequency f(Hz)	Wavelength λ(mm)	Theoretical ξ_t(m^{-1})	Measured ξ_m(m^{-1})	Surface condition clean/surfactant
12	19.52	1.21	6.32	Clean
12	17.93	1.74	7.48	TX-100
24	10.48	3.00	7.34	Clean
24	8.89	5.13	11.44	TX-100
36	7.56	4.91	10.84	Clean
36	6.37	8.42	13.37	TX-100

Table 1. Spatial decay rate comparison.

experience a more pronounced enhancement in wave decay due to surfactants, this trend is less evident in the experimental measurements. This is because the theoretical model accounts only for the change in surface tension, and smaller waves are more sensitive to it. It should be noted that merely altering the surface tension does not directly enhance energy dissipation, as surface tension itself is not a dissipative mechanism. The observed increase in the spatial decay rate, denoted by ξ, reflects spatial rather than temporal attenuation. In other words, within the theoretical model, surfactants do not increase dissipation; instead, they modify the wavelength and group velocity, resulting in faster spatial decay of the wavefield. However, real-world scenarios involve additional mechanisms caused by surfactants – such as alterations to subsurface flow patterns – that can substantially influence wave dissipation, even in larger waves (e.g. at 12 Hz) where changes in surface tension are less influential. These aspects will be examined in more detail in the following section. It should be noted that, in the 12 Hz cases, energy is leaked to superharmonic components, as evidenced by the wave profile and wavenumber spectra (figure 4). This energy leakage at 12 Hz causes the primary wave crest to decay more rapidly. As the decay estimation method is based on local peak amplitudes, the additional energy carried by superharmonic components is not explicitly resolved. Superharmonics are more prominent in the 12 Hz waves than in the higher-frequency cases examined in this study; the resulting ξ_m is larger, causing a larger discrepancy between the theoretical and measured values compared with the higher-frequency cases. Subharmonics and other low-frequency components from nonlinear wave–wave interactions (possibly resonant triads with spatial spread) are also present in the 36 Hz spectra. The wave profiles exhibit slight peak modulation. While these features are less pronounced than the superharmonics observed at 12 Hz, they can still affect the accuracy of ξ_m. Thus, the ξ_m values in table 1 should be viewed as indicators of enhanced dissipation in the surfactant-laden cases rather than precise estimates of the true dissipation rate.

3.3. *Surface particle trajectories*

Velocity fields beneath the free surface were obtained using PIV. Figure 6 shows the results for 12 Hz waves, resolved to a depth of approximately 3 mm. With interrogation windows of 32 $\times$ 32 pixels containing on average approximately five tracer particles, the PIV resolution is sufficient to reliably capture velocity field and velocity gradients. A 75 % interrogation window overlap is applied, resulting in a vector spacing of eight pixels; this increases the sampling density for numerical differentiation, while the true spatial resolution remains set at the 32 $\times$ 32 pixel window size. It is evident that in the presence of surfactants, the vertical velocity components become more pronounced, particularly on the rear face of the wave. Moreover, the velocity gradient of the vertical component is noticeably larger with surfactant addition. This is reflected in the velocity

https://doi.org/10.1017/jfm.2025.10982 Published online by Cambridge University Press

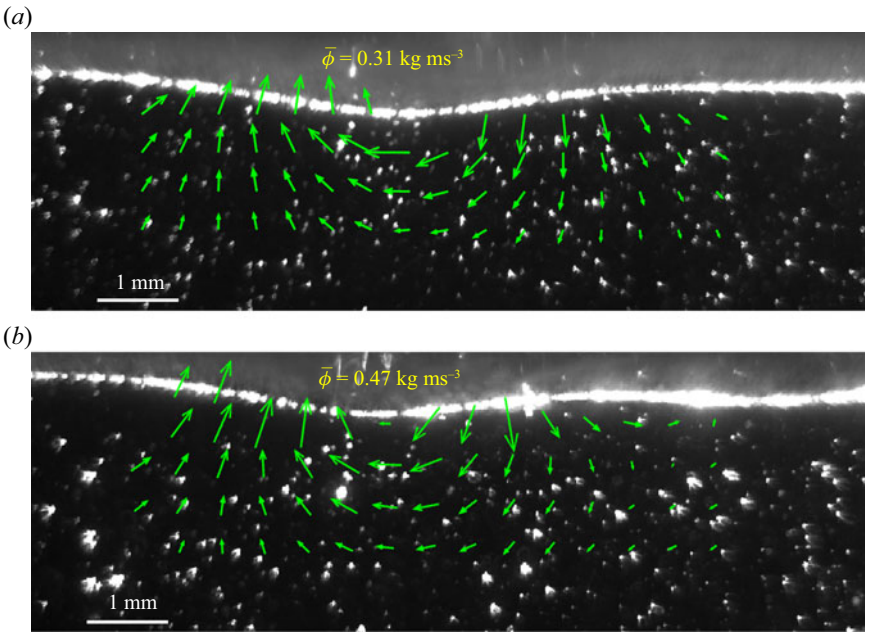


Figure 6. Velocity fields beneath 12 Hz waves: (*a*) clean water, (*b*) water with Triton X-100.

field plot, where the amplitude of the vertical velocity decays more rapidly with depth in figure 6(*b*) compared with the surfactant-free case in figure 6(*a*). These observations suggest a pronounced alteration in surface-particle motion due to the presence of surfactants. For particles located further below the surface, the differences between them are less pronounced.

To characterise the surface flow in more detail, a particle tracking approach is employed. These particles, visible as high-intensity regions in the recorded images, serve as Lagrangian markers of the surface fluid motion. A series of sequential local images of near-surface particles (as shown in figure 7) are acquired to capture their motion. Each image is first converted to greyscale, and a Gaussian smoothing filter is applied to reduce noise. A fixed intensity threshold, set at 70 % of the maximum intensity, is then used to segment the bright particle regions. Centroid positions of the detected particles are extracted from each frame using connected-component labelling. The particles are then linked across consecutive frames using a nearest-neighbour matching approach: for each particle in frame n, the distances to all particles in frame $n+1$ are computed, and the closest match is assigned, provided the displacement falls below a predefined threshold. This produces continuous two-dimensional trajectories for each particle over time. The trajectories of surface particles beneath 12 Hz waves, along with the recorded images, are shown in figure 7. It should be noted that at the high particle concentrations required for PIV, clustering and surface reflections can make it difficult to accurately distinguish individual particles. To address this, particle tracking is performed only in near-surface regions where the concentration is sufficiently low and particles are well isolated. Accordingly, the overall particle concentration in the surface tracking experiments is reduced compared with that used in the PIV measurements.

To evaluate the accuracy of the particle tracking method, the particle trajectories are compared with the wave profiles measured using the FS-SS method. At specific locations, particle displacement is compared with the corresponding wave height obtained from FS-SS measurements. The experiments are conducted at a fixed wavemaker stroke and

https://doi.org/10.1017/jfm.2025.10982 Published online by Cambridge University Press

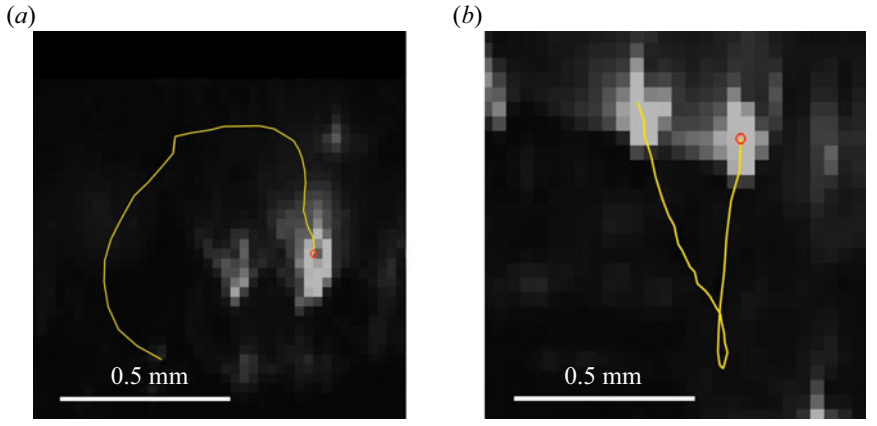


Figure 7. Near-surface particle trajectories of 12 Hz waves: (*a*) clean water, (*b*) with Triton X-100. Reference lengths are indicated in the panels.

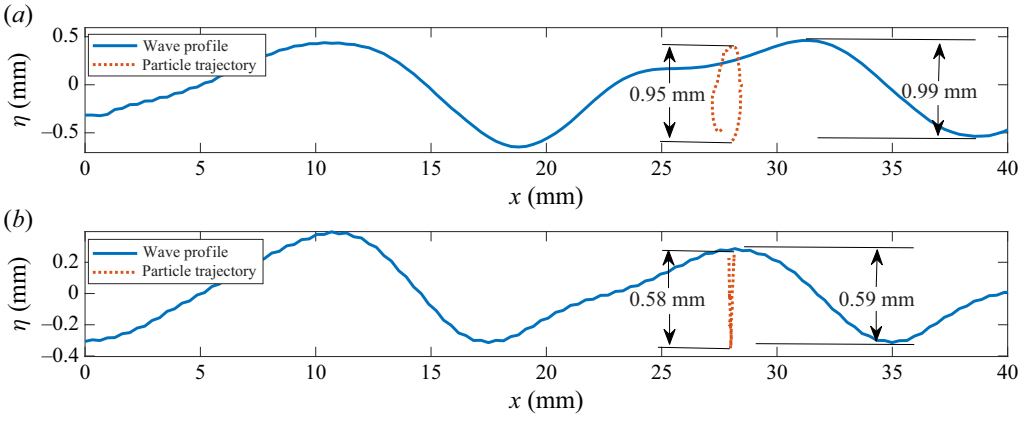


Figure 8. Wave profiles and particle trajectories of 12 Hz waves: (*a*) clean water, (*b*) water with Triton X-100. Solid lines, wave profiles; dashed lines, near-surface particle trajectories. Note that the ordinate scales differ.

frequency, with two runs performed for each case – one using FS-SS and the other using particle tracking. As illustrated in figure 8, results for 12 Hz waves in both clean water and water with added Triton X-100 show that the wave heights measured by particle tracking closely match those obtained using FS-SS at the same locations. The particle used in this comparison is located upstream of those shown in figures 7 and 9, and therefore exhibits a higher wave height. These findings confirm that both techniques provide comparable accuracy in representing the wave motion.

The surface particle trajectories of 12 Hz, 24 Hz and 36 Hz waves are shown in figure 9. Note that the scales in the figure differ because higher-frequency waves exhibit much smaller spatial dimensions. To facilitate comparison across different scales, a normalised trajectory is presented in figure 10. The length scale is normalised by dividing the position by the corresponding wavelength, and the trajectory is shifted such that its centre aligns with the origin. As can be seen, on the clean surface, the particle trajectories follow a circular motion, slightly distorted due to wave nonlinearity and measurement noise. The dip observed in the wave profile in § 3, attributed to the presence of superharmonics, is also evident in the surface particle trajectories. This observation is consistent with classic wave theory, which predicts that particles on the wave surface move in circular orbits.

https://doi.org/10.1017/jfm.2025.10982 Published online by Cambridge University Press

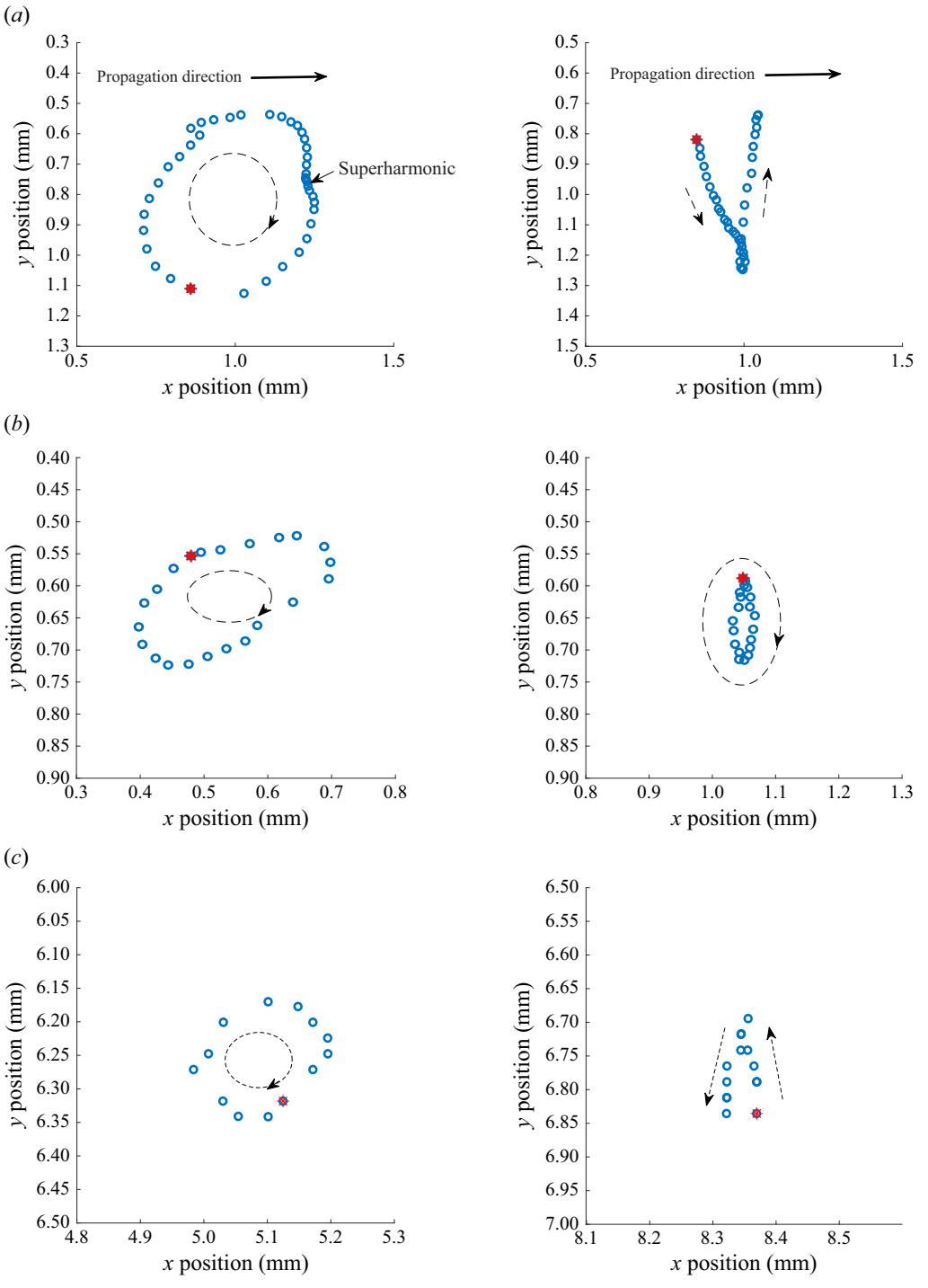


Figure 9. Surface particle trajectories over one wave period. Left column, clean water; right column, water with Triton X-100. (*a*) 12 Hz, (*b*) 24 Hz, (*c*) 36 Hz. The red star indicates the initial particle location. (Note that the scales differ).

https://doi.org/10.1017/jfm.2025.10982 Published online by Cambridge University Press

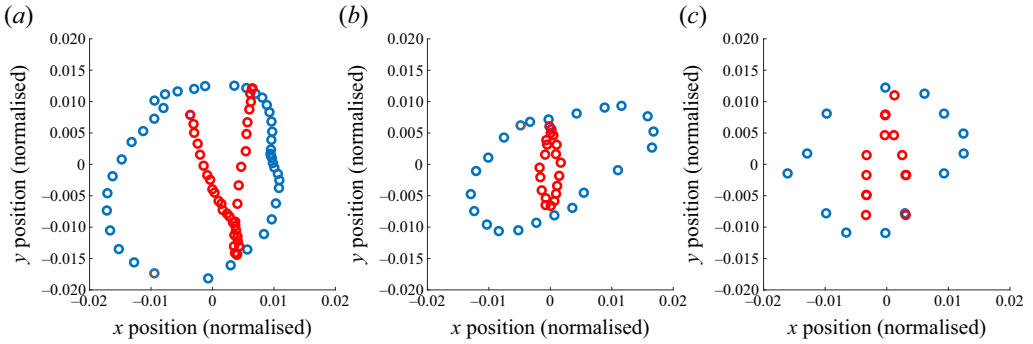


Figure 10. Normalised surface particle trajectories over one wave period. Blue circles, clean water; red circles, Triton X-100 solution. (*a*) 12 Hz, (*b*) 24 Hz, (*c*) 36 Hz.

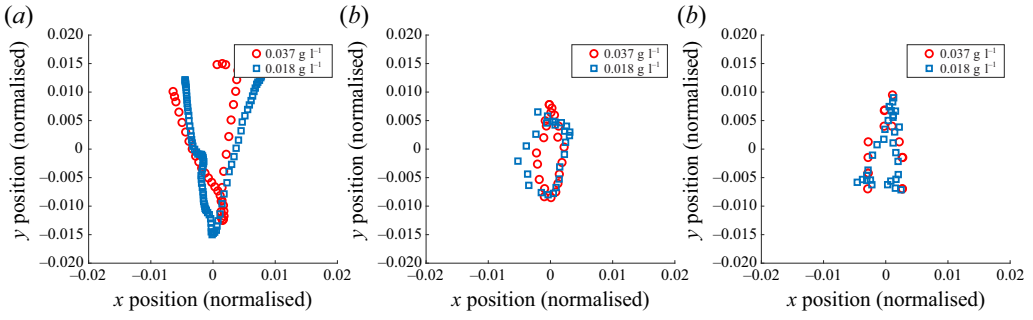


Figure 11. Normalised surface particle trajectories over one wave period, under two Triton X-100 concentrations. Red circles, 0.037 g l^{-1}; blue square, 0.018 g l^{-1}. (*a*) 12 Hz, (*b*) 24 Hz, (*c*) 36 Hz.

However, in the case with surfactant, the surface particles exhibit significantly different motion patterns. For 12 Hz waves, the presence of the surfactant prevents the particles from following a circular trajectory. Rather, particle motion becomes a combination of vertical oscillation and horizontal drift. In the 24 Hz cases, the particle trajectories form elliptical-like shapes. The particle trajectories at two different Triton X-100 concentrations are shown in figure 11. The change in concentration from 0.018 g l^{-1} to 0.037 g l^{-1} does not alter the particle trajectory significantly, indicating that other surface properties, such as surface viscosity, play only a minor role in determining the surface flow pattern. Rather, the Marangoni effect, which depends not on the absolute surfactant concentration but on the surface-tension gradient, dominates the alteration of the surface flow. The dissipation rate caused by viscosity on a unit volume of fluid in a two-dimensional flow can be written as

$$\phi = \mu \left[2 \left(\frac{\partial u}{\partial x} \right)^2 + 2 \left(\frac{\partial w}{\partial z} \right)^2 + \left(\frac{\partial w}{\partial x} + \frac{\partial u}{\partial z} \right)^2 \right], \tag{3.4}$$

where μ is the dynamic viscosity of water, and u, w are the x and z component velocities, respectively. As shown in (3.4), the dissipation is proportional to the square of the velocity gradient. Consequently, altering the flow pattern from circular to elliptical or vertical increases velocity gradients such as $\partial u/\partial x$ and $\partial w/\partial z$, thereby enhancing the overall dissipation rate. Using the velocity field obtained from the PIV data, the dissipation rate ϕ is calculated throughout the resolved flow field for both the clean water and Triton X-100

https://doi.org/10.1017/jfm.2025.10982 Published online by Cambridge University Press

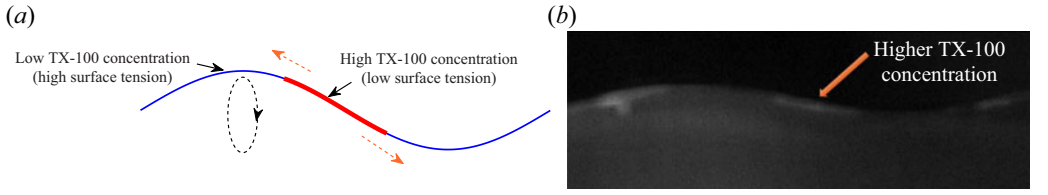


Figure 12. (*a*) Conceptual diagram of surface flow with surfactants; red highlights regions of high surfactant concentration, black dashes with an arrow show distorted particle paths, and red dashed arrows indicate Marangoni flows. (*b*) Nile Red fluorescence image, where brighter regions correspond to higher concentration.

cases, and the spatially averaged values $\bar{\phi}$ are shown in figure 6. The results demonstrate that the addition of surfactant leads to a significant increase in the dissipation rate.

The results in this study are consistent with very recent numerical predictions of Panda *et al.* (2025), who showed that Marangoni stresses arising from surfactant gradients can oppose inertial flows, effectively 'rigidifying' the interface; the numerical simulations in Panda *et al.* (2025) assumes the surfactant is insoluble. An experimental study by Strickland *et al.* (2015) demonstrated the determination of insoluble surfactant concentrations at the air–water interface using fluorescence of 7-nitrobenz-2-oxa-1,3-diazol-4-yl-tagged phosphatidylcholine, under Faraday waves. For soluble surfactants such as Triton X-100 used in the present work, direct tracking of the surface concentration is more challenging. A preliminary attempt is made in this study to visualise the spatial distribution of Triton X-100 at the air–water interface under 12 Hz waves. Nile Red is employed as a fluorescent probe due to its preferential partitioning into hydrophobic environments, enabling co-localisation with Triton X-100 films at the interface. In non-polar media, it exhibits strong red fluorescence with an emission maximum near 600 nm when excited by blue light (488–520 nm). In the experiments, methanol-based Nile Red is first dispersed in the bulk water, followed by the addition of a Triton X-100 stock solution. During the initial mixing stage, Triton X-100 is distributed transiently throughout the bulk, and its distribution is clearly visualised under blue laser illumination, confirming the efficacy of Nile Red as a tracer. Within approximately 30–60 s, Triton X-100 accumulated at the air–water interface and formed a coherent surface layer. The resulting fluorescence is captured using the high-speed imager, a long-pass filter (LP590-52, MidOpt) installed in front of the camera to reject scattered excitation light and isolate the red emission light. In the recorded image (figure 12*b*), regions of higher fluorescence intensity correspond to higher Triton X-100 concentrations. The results reveal a spatially inhomogeneous distribution of surfactants, with higher concentrations in the regions between the crest and trough, where the free surface experiences compression. Although further refinement of the experimental technique is needed, particularly to address the insufficient fluorescence intensity for high-speed imaging and the lack of time-resolved distributions, our findings demonstrate that surfactants distribute non-uniformly, leading to surface-tension gradients on the surface, and show that Nile Red is a promising probe for future quantitative investigations. Due to the complexity involved in preparing an insoluble surfactant monolayer, their investigation is reserved for future work.

It should be noted that, for the 36 Hz waves, the motion is similar to that observed in the 12 Hz cases, but rather than exhibiting a forward drift, the particles appear to drift backward. The theoretical Stokes drift velocity of surface particles can be estimated by $\bar{u}_t = (ka)^2 C$, where a is the wave amplitude, and C is the phase velocity. The drift velocities are measured using the recorded image frames. As the wave propagates and its steepness decreases, the drift velocity is expected to decrease. In this study, the measured drift velocities $\bar{u}_m$ are quantified as the mean horizontal particle velocities in five full wave

https://doi.org/10.1017/jfm.2025.10982 Published online by Cambridge University Press

Cases	Wave height H(mm)	Wavelength λ(mm)	Initial steepness ka	Predicted drift $\bar{u}_t$(mm s^{-1})	Measured drift $\bar{u}_m$(mm s^{-1})
12 Hz, clean	1.10	19.52	0.18	4.18	4.38 ± 0.28
12 Hz, TX-100	0.90	17.93	0.16	2.90	2.26 ± 0.19
24 Hz, clean	0.39	10.48	0.12	2.44	2.35 ± 0.07
24 Hz, TX-100	0.28	8.89	0.10	1.28	0.48 ± 0.04
36 Hz, clean	0.26	7.56	0.11	2.61	2.44 ± 0.12
36 Hz, TX-100	0.17	6.37	0.08	0.95	-0.52 ± 0.09

Table 2. Surface particle drift comparison.

periods. For comparison, the theoretical prediction accounts for the spatial decay of ka, by using the experimentally measured decay rate. For instance, in 12 Hz clean water, ka decreases by approximately 11 % after one wavelength and by 45 % after five periods. The theoretical drift velocity $\bar{u}_t$ is then calculated by averaging the Stokes drift over this five-period span. It is worth noting that, within five periods, fluid particles do not drift a significant distance. For example, in the case of 12 Hz waves, the particle drift over five periods was approximately 1.7 mm, which corresponds to less than one-tenth of a wavelength. Thus, the spatial amplitude decay has only a minor influence on the mean drift velocity. The results are summarised in table 2. Five measurements are performed for each case, and the mean value together with its uncertainty is reported in the last column of table 2. The uncertainty, σ_u, is calculated using $\sigma_u = \sigma/\sqrt{N}$, where σ is the standard deviation and N is the number of measurements ($N = 5$ in this study). As shown in table 2, for the clean-water cases, the measured drift velocities closely match the theoretical predictions. In contrast, for surfactant-laden cases, the measured velocities are consistently lower than the predicted values. This discrepancy becomes more pronounced at higher frequencies, indicating that the presence of surfactants increasingly suppresses horizontal motion. This is attributed to Marangoni flows induced by surface-tension gradients. As the wave frequency increases, the effect becomes more pronounced. At sufficiently high frequencies, the Marangoni effect becomes dominant, eventually overcoming the wave-induced Stokes drift and reversing the net surface particle motion (negative drift velocity at 36 Hz). This is discussed in detail in the following section.

3.4. *Marangoni effects on surface flow with waves*

The deformation of the free surface (waves) leads to non-uniform surfactant concentrations, with the concentration reduced at both wave crests and troughs. Regions of higher surfactant concentration correspond to lower surface tension, whereas regions of lower surfactant concentration correspond to higher surface tension. The resulting surface-tension gradient drives flow from the lower-surface-tension region toward the higher-surface-tension region, which is the called Marangoni effect. This induced surface flow opposes the wave-driven horizontal particle motion, transforming roughly circular trajectories into elliptical ones. This phenomenon was theoretically predicted for water waves with insoluble surfactants (Manikantan & Squires 2020), and is shown qualitatively in figure 12. This Marangoni stress is more pronounced in shorter waves, as their shorter crest-to-trough distance produces a larger surface-tension gradient.

For soluble surfactants (such as Triton X-100 in this study), surface-tension gradients induced by surface deformation can be compensated by adsorption and desorption processes. If the surfactant concentration at the interface remains in rapid equilibrium with the bulk solution, the resulting surface-tension gradient is typically insufficient to

https://doi.org/10.1017/jfm.2025.10982 Published online by Cambridge University Press

generate noticeable Marangoni flows. However, if adsorption and desorption are slow, such that the number of surfactant molecules at the interface remains nearly constant during deformation, the surface behaves similarly to that of an insoluble surfactant. In this case, Marangoni flows suppress the horizontal motion of surface fluid particles. As the wave scales decrease, the Marangoni effect becomes increasingly significant, eventually causing the surface motion to become predominantly vertical. In this limit, the free surface behaves like an incompressible sheet (Manikantan & Squires 2020).

A surface-tension gradient along the air–water interface generates a tangential Marangoni stress. The interfacial stress boundary condition (assuming a one-dimensional surface) is

$$\mu \frac{\partial u}{\partial z}\bigg|_{z=0} = \frac{\partial T}{\partial x}, \tag{3.5}$$

where μ is the dynamic viscosity, u is the surface–parallel velocity (for small wave steepness, assumed horizontal), and T is surface tension. Scaling the gradients as $\partial u/\partial z \sim U_M/h$ gives

$$U_M \sim \frac{h}{\mu}\frac{\partial T}{\partial x}, \tag{3.6}$$

where h is the viscous penetration depth within the subphase, i.e. the depth over which the Marangoni stress drives shear. For oscillatory flow this depth is

$$h = \sqrt{\frac{2\nu}{\omega}}, \tag{3.7}$$

where ν is the kinematic viscosity and ω is the wave frequency.

Wave-induced convergence or divergence along the interface perturbs the interfacial concentration Γ, producing a dynamic surface-tension gradient:

$$\frac{\partial T}{\partial x} \approx E\frac{\partial(\delta\Gamma/\Gamma)}{\partial x}, \tag{3.8}$$

where E is the dilational (Marangoni) elasticity, which changes with oscillating frequency, and $\delta\Gamma$ denotes the change in surfactant concentration. To relate wave-driven surface motion to surfactant redistribution, the surfactant conservation equation for a (locally) insoluble interface is used (neglecting surface diffusion):

$$\frac{\partial(\delta\Gamma)}{\partial t} + \Gamma_0\frac{\partial u}{\partial x} \approx 0, \tag{3.9}$$

where Γ_0 is the initial surfactant concentration and u is the wave-induced surface velocity with the order $u \sim a\omega$. Noting that the concentration oscillates at frequency ω and u varies spatially with k, we obtain

$$\frac{\delta\Gamma}{\Gamma_0} \sim \frac{1}{\omega}\left|\frac{\partial u}{\partial x}\right| \sim \frac{1}{\omega}(ka\omega) = ka. \tag{3.10}$$

Hence, the relative concentration variation induced by the surface wave is

$$\frac{\delta\Gamma}{\Gamma_0} = O(ka). \tag{3.11}$$

As this variation occurs over a distance of order $1/k$ (one wavelength), the surface gradient of the concentration field scales as

$$\left|\frac{\partial}{\partial x}\left(\frac{\delta\Gamma}{\Gamma_0}\right)\right| \sim k(ka) = k^2a, \tag{3.12}$$

https://doi.org/10.1017/jfm.2025.10982 Published online by Cambridge University Press

hence,

$$U_M \sim \frac{h}{\mu} E\, k^2 a. \tag{3.13}$$

For a two-dimensional regular wave, the characteristic scale of the velocity of surface particles is $U_W \sim a\omega$, and the ratio U_M/U_W therefore quantifies the relative strength of the Marangoni-driven flow compared with the wave-induced motion. Determining the dilational (Marangoni) elasticity E requires measurements that are beyond the scope of the present experimental set-up. Rather, values of the dynamic Marangoni elasticity of Triton X-100 in the literature (Langevin 2014; Ma *et al.* 2025) are used as a rough estimation; the value range is 10–50 mN m^{-1}. For water ($\nu = 10^{-6}$ m^2 s^{-1}) driven at 12 Hz ($\omega = 75.36$ rad s^{-1}), we obtain $h \approx 1.6$ mm. Substituting these values into the scaling estimate yields the ratio $U_M/U_W \sim O(1)$. Therefore, Marangoni flow is sufficiently strong to compete with the wave-induced particle motion and, over multiple wave periods, may alter or even reverse the net drift direction. It should be noted that the calculation presented here is only a coarse estimate. Detailed measurements are required to quantitatively compare the Marangoni flow velocity with the wave-induced velocities.

As Triton X-100 is a soluble surfactant, the adsorption and desorption processes may re-balance the surface-tension gradient. Yet, the experimental results in the present study match the predicted elliptical-like particle motion for insoluble surfactant (especially in the 24 Hz case). This is because dynamic surface-tension data indicate diffusion-controlled adsorption of Triton X-100 with characteristic times of >0.05–200 s at the air–water interface (Fainerman *et al.* 2009*a*,*b*; Gassin *et al.* 2012). Our wave frequencies/periods (12–36 Hz/0.083–0.028 s) are comparable to or shorter than these times, so adsorption cannot equilibrate within each cycle and thus is slow relative to the wave motion. Moreover, the amphiphilic nature of Triton X-100 promotes its adsorption at the air–water interface. Under these conditions, the interface behaves similarly to that of an insoluble monolayer. The results in this study provide clear experimental evidence that Marangoni effects significantly alter surface flow patterns beneath small-scale waves, transforming the typical circular motion into elliptical or even near-linear trajectories. This modification increases the shear stress between the surface layer and the fluid immediately below, resulting in enhanced dissipation rates.

4. Conclusions

The experiments demonstrate enhanced energy dissipation in the presence of surfactants. The measured dissipation rates in clean water exceed predictions from viscous linear wave theory, likely due to nonlinearity/superharmonics, and sidewall contact line friction. Experimental evidence suggests that the dissipation enhancement caused by surfactants arises (at least partly) from substantial modifications to the free-surface flow. This influence becomes significant even before the wave scale enters the capillary regime. In fact, relatively longer waves (e.g. 12 Hz) exhibit significant changes in surface particle trajectories and strong dissipation enhancement.

By tracking the trajectories of surface particles, it is observed that surfactants substantially alter surface motion, particularly in the horizontal direction. Instead of exhibiting circular paths, particles follow elliptical-like or nearly linear vertical trajectories, with small net drift per wave cycle. Surface-tension gradients arising from wave-induced deformations generate a surface flow that opposes the underlying fluid motion. This counter-flow alters the particle motion and increases velocity gradients at the surface, thereby enhancing viscous dissipation. These findings are supported by PIV

https://doi.org/10.1017/jfm.2025.10982 Published online by Cambridge University Press

measurements and particle tracking data, confirming that surfactant-induced surface flow modifications are a key mechanism for the enhanced dissipation by surfactants.

In the present study, the Triton X-100 concentrations are well below the CMC, ensuring that the surfactant adsorbs primarily at the interface rather than forming micelles in the bulk water. Under these conditions, increasing the Triton X-100 concentration does not alter the near-surface particle motion patterns. This suggests that changes in surface tension or surface viscosity are not the primary mechanisms governing the alteration of particle motion, rather, it is the gradient in surface tension that changes the behaviour. At the wave frequencies examined, the adsorption–desorption dynamics of the Triton X-100 surfactant are not rapid enough to maintain a uniform surface concentration. Consequently, surface-tension gradients develop, leading to Marangoni flows – behaviour typically attributed to insoluble surfactants. These results demonstrate that soluble surfactants can also induce significant Marangoni effects in small-scale waves, contributing to energy dissipation through altered surface flow patterns. Moreover, the presence of surfactants suppresses the Stokes drift due to the opposing surface flow generated by the Marangoni effect. At higher wave frequencies, this Marangoni-driven flow becomes dominant, reversing the direction of net surface particle drift.

Supplementary movies. Supplementary movies are available at https://doi.org/10.1017/jfm.2025.10982.

Declaration of interests. The authors report no conflict of interest.

References

Benetazzo, A., Cavaleri, L., Ma, H., Jiang, S., Bergamasco, F., Jiang, W., Chen, S. & Qiao, F. 2019 Analysis of the effect of fish oil on wind waves and implications for air–water interaction studies. *Ocean Sci.* **15** (3), 725–743.

Cox, C.S., Zhang, X. & Duda, T.F. 2017 Suppressing breakers with polar oil films: using an epic sea rescue to model wave energy budgets. *Geophys. Res. Lett.* **44** (3), 1414–1421.

Crapper, G.D. 1984 *Introduction to Water Waves*. Ellis Horwood Limited Press.

Fainerman, V.B., Lylyk, S.V., Aksenenko, E.V., Liggieri, L., Makievski, A.V., Petkov, J.T., Yorke, J. & Miller, R. 2009*a* Adsorption layer characteristics of triton surfactants: part 2. dynamic surface tension and adsorption. *Colloids Surf. A: Physicochem. Engng Aspects* **334** (1–3), 8–15.

Fainerman, V.B., Lylyk, S.V., Aksenenko, E.V., Makievski, A.V., Petkov, J.T., Yorke, J. & Miller, R. 2009*b* Adsorption layer characteristics of Triton surfactants: 1. Surface tension and adsorption isotherms. *Colloids Surf. A: Physicochem. Engng Aspects* **334** (1–3), 1–7.

Ferrero, L., *et al.* 2022 Airborne and marine microplastics from an oceanographic survey at the Baltic Sea: an emerging role of air-sea interaction? *Sci. Total Environ.* **824**, 153709.

Gassin, P.-M., Martin-Gassin, G., Meyer, D., Dufrêche, J.-F. & Diat, O. 2012 Kinetics of Triton-x100 transfer across the water/dodecane interface: analysis of the interfacial tension variation. *J. Phys. Chem.* **116** (24), 13152–13160.

Lamb, H. 1924 *Hydrodynamics*. University Press.

Langevin, D. 2014 Rheology of adsorbed surfactant monolayers at fluid surfaces. *Annu. Rev. Fluid Mech.* **46** (1), 47–65.

Levich, V.G. & Krylov, V.S. 1969 Surface-tension-driven phenomena. *Annu. Rev. Fluid Mech.* **1** (1), 293–316.

Ma, G., Gong, Q., Xu, Z., Jin, Z., Zhang, L., Ma, G. & Zhang, L. 2025 The interfacial dilational rheology of surfactant solutions with low interfacial tension. *Molecules* **30** (3), 447.

Manikantan, H. & Squires, T.M. 2020 Surfactant dynamics: hidden variables controlling fluid flows. *J. Fluid Mech.* **892**, P1.

Martínez-Vicente, V., *et al.* 2019 Measuring marine plastic debris from space: initial assessment of observation requirements. *Remote Sens.* **11** (20), 2443.

Matsuda, K., Komori, S., Takagaki, N. & Onishi, R. 2023 Effects of surface tension reduction on wind-wave growth and air–water scalar transfer. *J. Fluid Mech.* **960**, A22.

Moisy, F., Rabaud, M. & Salsac, K. 2009 A synthetic Schlieren method for the measurement of the topography of a liquid interface. *Exp. Fluids.* **46** (6), 1021–1036.

https://doi.org/10.1017/jfm.2025.10982 Published online by Cambridge University Press

PANDA, D., KAHOUADJI, L., TUCKERMAN, L.S., SHIN, S., CHERGUI, J., JURIC, D. & MATAR, O.K. 2025 Marangoni-driven patterns, ridges and hills in surfactant-covered parametric surface waves. *J. Fluid Mech.* **1008**, R4.

PONCE-TORRES, A., VEGA, E.J. & MONTANERO, J.M. 2016 Effects of surface-active impurities on the liquid bridge dynamics. *Exp. Fluids.* **57** (5), 67.

POPINET, S. 2018 Numerical models of surface tension. *Annu. Rev. Fluid Mech.* **50**, 49–75.

RAJAN, G.K. 2020 A three-fluid model for the dissipation of interfacial capillary-gravity waves. *Phys. Fluids* **32** (12), 122121.

SERGIEVSKAYA, I., ERMAKOV, S., LAZAREVA, T. & GUO, J. 2019 Damping of surface waves due to crude oil/oil emulsion films on water. *Mar. Pollut. Bull.* **146**, 206–214.

SHEN, L., DENNER, F., MORGAN, N., VAN WACHEM, B. & DINI, D. 2018 Capillary waves with surface viscosity. *J. Fluid Mech.* **847**, 644–663.

Sigma-Aldrich 2025 Triton^{TM} x-100 product information sheet: Product Numbers x-100, T9284, T8787, T8532. Sigma-Aldrich, Inc. Available at: https://www.sigmaaldrich.com/deepweb/assets/sigmaaldrich/product/documents/160/855/t8532pis.pdf, accessed 16 September 2025.

SOBHANI, A., SIADATMOUSAVI, S.M. & MEHDINIA, A. 2024 Surface microplastics dynamics in the Persian Gulf and Arabian Sea using numerical modelling and CYGNSS satellite estimations. *Mar. Environ. Res.* **202**, 106749.

STRICKLAND, S.L., SHEARER, M. & DANIELS, K.E. 2015 Spatiotemporal measurement of surfactant distribution on gravity–capillary waves. *J. Fluid Mech.* **777**, 523–543.

SUN, Y., BAKKER, T., RUF, C. & PAN, Y. 2023 Effects of microplastics and surfactants on surface roughness of water waves. *Sci. Rep.* **13** (1), 1978.

XU, C. & PERLIN, M. 2021 Gravity–capillary multi-component wave patterns generated by a single-frequency wave-maker oscillation and subsequent resonances. *J. Fluid Mech.* **926**, A39.

XU, C. & PERLIN, M. 2023 Parasitic waves and micro-breaking on highly nonlinear gravity–capillary waves in a convergent channel. *J. Fluid Mech.* **962**, A46.

https://doi.org/10.1017/jfm.2025.10982 Published online by Cambridge University Press